Fluorinated Ni-O-C Heterogeneous Catalyst for Efficient Urea-Assisted Hydrogen production

Xuefei Xu[1#], Habib Ullah[2#], Muhammad Humayun[1], Linfeng Li[1], Xia Zhang[1],

Damien P. Debecker[3], Kaifu Huo[1,4], Chundong Wang[1]*

1. School of Integrated Circuits, Wuhan National Laboratory for Optoelectronics, Huazhong University of Science and Technology, Wuhan 430074, P. R. China

2. Department of Engineering, Faculty of Environment, Science and Economy, University of Exeter, EX4 4QF, United Kingdom

3. Institute of Condensed Matter and Nanosciences (IMCN), UCLouvain, 1348 Louvain-La-Neuve, Belgium

4. Research Institute of Huazhong University of Science and Technology in Shenzhen, Shenzhen 518063, P. R. China

* Email: apcdwang@hust.edu.cn

Abstract

Constructing multiple heterogeneous structures allows improving the electrocatalytic activity of NiO by incorporating multiple active sites. Unfortunately, the poor conductivity of NiO makes efficient charge transfer within the heterogeneous structures difficult, thereby inhibiting the improvement of its intrinsic activity. Herein, F-doped NiO/Ni@C heterogeneous catalyst (F-NiO/Ni@C) is fabricated via a new organic-inorganic hybrid approach, showing both advanced hydrogen evolution reaction (HER) and urea oxidation reaction (UOR) activity. The targeted F-doping increases electron delocalization, and facilitates electron transfer from Ni to NiO at the nano-interfaces. This interphase synergy provides ready-to-use F-NiO active sites, allowing F-NiO/Ni@C to achieve optimum H* adsorption Gibbs free energy for HER and a lower energy barrier for UOR. As a result, the as-configured F-NiO/Ni@C || F-NiO/Ni@C cell requires an ultra-low cell voltage of 1.37 V to achieve $10 \, \mathrm{mA \, cm^{-2}}$ in alkaline media (with 0.3M urea), outperforming the state-of-the-art benchmark Pt/C|| RuO_2 cell (1.45 V). This work reveals the positive impact of anion doping on interphase synergy and provides useful guidelines for designing monometallic catalysts for UOR as well as hydrogen generation.

1. Introduction

Hydrogen production has received a great deal of interest as a remedy to the depletion of traditional fossil fuels[1]. Compared to the traditional steam reforming and coal gasification strategies, electrocatalytic water splitting has been recognized as a sustainable approach because of obvious benefits of zero carbon emissions, high product purity, and low cost[2]. Water splitting involves two half-cell reactions, i.e. the hydrogen evolution reaction (HER) occurring at the cathode and oxygen evolution reaction (OER) happening at the anode. Unfortunately, anodic OER greatly inhibits the

overall water-splitting efficiency because of its high thermodynamic potential (1.23 V) and slow reaction kinetics[3]. Noteworthy, the UOR (i.e., $CO(NH_2)_2 + 6OH^- \rightarrow N_2 + CO_2 + 5H_2O + 6e^-$) has a lower thermodynamic potential of 0.37 V with respect to OER, and has therefore been considered as an appropriate alternative anodic reaction[4]. Additionally, urea is decomposed into nontoxic N_2 and CO_2 during the UOR process, allowing to purify the urea-rich wastewater from another perspective [5]. The UOR occurs through a complicated six-electron transfer process with several complex intermediates adsorption and desorption activity, however, the urea-assisted H_2 generation system has yet to demonstrate a successful scenario sufficiently endowing the fulfill practical demand[6]. As such, developing low-cost, high-efficiency electrocatalysts to accomplish advanced UOR and HER is crucial.

Noble metal-based catalysts (e.g., Pt, IrO_2, and RuO_2) have been proven to exhibit high catalytic activity for UOR, similar to those employed in HER, but are confronted to the challenge of high cost and scarcity[7]. Recently, high oxidation current densities for UOR have been demonstrated for Ni-based catalysts such as Ni-based alloys, oxides, hydroxides, phosphides, and sulfides, where the Ni^{3+} species acts as the catalytically active centers[8]. Among the mentioned Ni-based catalysts, NiO has garnered much interest because of its environmental friendliness, cost effectiveness, and high corrosion resistance. However, the electrocatalytic activity of pristine NiO is still far away from satisfactory. The reason could be attributed to the fact that Ni^{2+} ($t_{2g}^6 e_g^2$) possess high e_g occupancy, leading to a strong binding with the reaction intermediates, and then resulting in favorable desorption of gaseous products. To optimize the adsorption and desorption of the reaction intermediates, interface engineering has been proposed as a valid strategy[9]. It was reported that transition metals/transition metal oxides (TM/TMO) heterojunction could weaken the H* absorption of TMO, in turn boosting

the alkaline HER kinetics[10]. Multilayer heterogeneous structure endows TM/TMO with optimized d-band center, leading to advanced UOR activity[11]. Unfortunately, NiO generally possess poor conductivity due to the entangled internal structure, which may impoverish the electron density at the interface.

Heteroatom doping (including metal[12] and nonmetal atom[13]) is thought to be an effective way for modulating the local charge redistribution in NiO. As reported by Qian et al. [12a], Co-doped NiO presents a higher electron occupied state at the Fermi level compared to the counterpart pure NiO, showing metallic-like characters. Similarly, Li et al. also demonstrated that S-doping can decrease the band gap of NiO from 3.01 to 2.74 eV[14]. Apart from the conductivity tailoring, the heteroatom doping can also create certain amount of oxygen vacancies in NiO, enabling to expose abundant active sites, thereby remarkably enhancing their electrocatalytic activities[15]. Nevertheless, developing a simple method to achieving controllable doping in NiO-based heterojunction structure and clarifying how to enhance its HER and UOR kinetics still remains challenging.

In this work, we proposed a simple organic-inorganic hybrid strategy to prepare an F-doped NiO/Ni@C heterojunction structure (F-NiO/Ni@C). Different from the traditional NH_4F decomposition method, the decomposition of fluorine-containing organic matter allow avoiding the generation of toxic HF while effectively achieving F doping. Our as-prepared F-NiO/Ni@C requires a low overpotential of 46 mV for HER and a potential of 1.31 V for UOR to achieve a current density of $mA\,cm^{-2}$ in an alkaline medium. In terms of overall urea splitting, the F-NiO/Ni@C || F-NiO/Ni@C cell has a potential of 1.37 and 1.57 V at 10 and 200 $mA\,cm^{-2}$, respectively, which outperforms the state-of-the-art Pt/C || RuO_2 cell. Furthermore, a favorable urea elimination rate of 94.86% is achieved by such an overall urea electrolyzer, which is 4.02 times higher

than that of pristine NiO/Ni@C. Theoretical calculations indicate that F-doping accelerates the electrons transfer from Ni to NiO, thereby promoting the intrinsic catalytic activity of NiO, leading to an optimal hydrogen adsorption Gibbs free energy for HER and reduced energy barrier for UOR.

Results and Discussion

Synthesis and structural characterization

The F-NiO/Ni@C catalyst was synthesized via our proposed two steps strategy as depicted in Figure 1. A solvothermal reaction was first performed in a three-phase system (DMF/ethanol/water), in which 4-Fluoro Salicylic Acid (F-H_2SA) organic molecules were successfully introduced into the interlayer of Ni(OH)$_2$, and subsequently Ni(OH)$_2$-FSA was formed. Next, the as-obtained Ni(OH)$_2$-FSA was subjected to an annealing treatment at 450 °C in Ar atmosphere, leading to the formation of NiO. During the annealing process, the F-H_2SA was first carbonized, and then the liberated F atoms should substitute part of the oxygen atoms in NiO due to their higher electronegativity[16], after which F-NiO/Ni@C was obtained. For comparison, NiO/Ni@C composite was also prepared with salicylic acid (H_2SA) serving as the intercalating organic molecule instead of F-H_2SA.
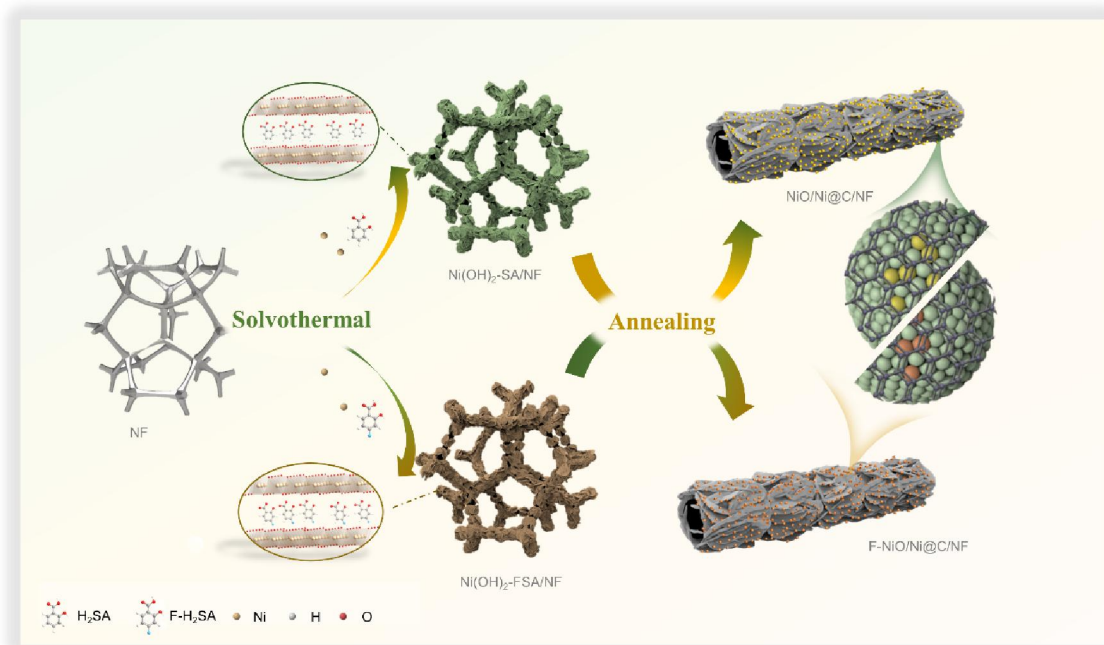
Figure 1. Schematic illustration of the synthesis procedure of NiO/Ni@C and F-NiO/Ni@C.

The successful incorporation of organic molecules (H_2SA or $F-H_2SA$) into the interlayer of $Ni(OH)_2$ was verified by Fourier transform infrared (FT-IR) spectroscopy. As depicted in Figure S1, the absorption peaks at 1498 cm^{-1} are associated to the stretching vibration of para-aromatic C-H group, while the peaks at 1577 and 1380 cm^{-1} arose from the asymmetric and symmetric vibrations of the coordinated carboxyl (-COO-) group, respectively[17]. Compared to the $Ni(OH)_2$-SA, the new peak at 1222 cm^{-1} in $Ni(OH)_2$-FSA belongs to the C-F bond, evidencing the successful incorporation of F dopant into the matrix[18]. To examine the crystalline structure of $Ni(OH)_2$-SA and $Ni(OH)_2$-FSA, X-ray diffraction (XRD) patterns were collected as well. One pronounced peak at 6.83° is discerned in sample $Ni(OH)_2$-SA, signifying that the interlamellar spacing has been increased to 1.28 nm, which unambiguously validates the successful intercalation of guest molecules into the matrix interlayer (Figure S2).

The layer thickness of Ni(OH)$_2$ is estimated to be 0.48 nm, while the simulated size of H$_2$SA molecules is predicted to be 0.91 nm, suggesting that the H$_2$SA is arranged with monolayer at a specific angle (Figure S3a, b). Due to the larger size of F-H$_2$SA (i.e., 0.96 nm), the Ni(OH)$_2$-FSA shows a lager interlayer distance of 1.36 nm ($2\theta_{(003)} = 6.46°$) compared to the Ni(OH)$_2$-SA (Figure S2 and S3c, d). Field emission scanning electron microscopy (FESEM) reveals that the Ni(OH)$_2$-SA and Ni(OH)$_2$-FSA nanosheet arrays are uniformly grown on the Ni foam (NF) (Figure S4-S5). Of note, F signal was also identified in the EDS spectra of Ni(OH)$_2$-FSA, which further confirms the successful incorporation of F dopant. It was noticed that F content in Ni(OH)$_2$-F$_x$SA (x=0.5/1.0/2.0) raised with the increase of the F-H$_2$SA amount introduced in the synthesis.
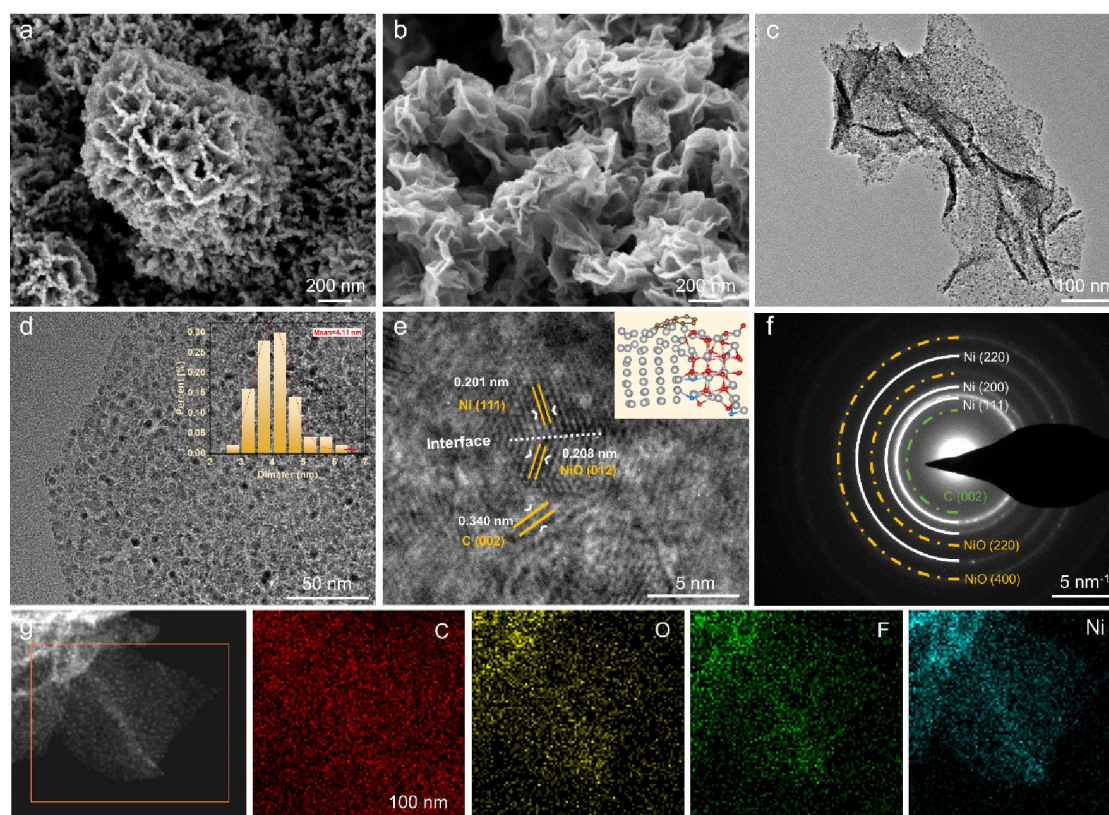

Figure 2. FESEM images of (a) NiO/Ni@C and (b) F-NiO/Ni@C. (c, d) TEM images of F-NiO/Ni@C together with the counterpart diameter analysis of dispersed nanoparticles on the nanosheets (inset of Figure 2d). HRTEM images (e) and SADE patterns (f) of F-NiO/Ni@C. (g) EDS mapping images of C, O, F, Ni elements of F-

NiO/Ni@C.

Figure 2a, b depicts SEM images of F-NiO/Ni@C, where curved nanosheets were observed. Compared to the precursor Ni(OH)$_2$-FSA, the surface of F-NiO/Ni@C is somewhat rougher. Transmission electron microscopy (TEM) was further used to examine the as-prepared sample. As shown in Figure S6a, b, it unveils the fact that NiO/Ni@C is composed of agglomerated nanoparticles (NPs) with an average particle size of 11 nm, which are wrapped in thin carbon layers. Similarly, F-NiO/Ni@C is also composed of NPs decorated in thin carbon layers, in which the size of uniformly distributed NPs was *ca.* 4.1 nm (Figure 2c, d). The small NPs could be possibly due to the fact that doped F has a different ion radius and charge number to that of O, which may cause internal stress, charge discrepancy, and lattice deformation in the NiO host, subsequently impeding NiO further growth[19]. The high-resolution TEM (HR-TEM) micrograph of F-NiO/Ni@C is shown in Figure 2e. The well-resolved lattice fringes of 0.201 and 0.208 nm are indexed to the (111) plane of Ni and (200) plane of NiO, respectively, which is fully consistent with NiO/Ni@C (Figure S6c)[10]. It is worth noting that oxidized and reduced Ni species generate localized hetero-interfaces at the nanoscale in a random way rather than long-range ones, exposing more active sites and accelerating reaction kinetics. On the other hand, the measured d-spacing of 0.340 nm could be attributed to the (002) plane of graphite carbon. In such a configuration where nanoparticles are embedded in a carbon layer, the latter stimulates nano-hetero-interfacing and increases the electronic conductivity of catalysts[20]. Figure 2f depicts the selected-area electron diffraction (SAED) patterns, where the concentric rings are indexed to the (220), (200) and (111) planes of Ni, (220) and (400) planes of NiO, and (002) planes of carbon, being in line with the SAED patterns of NiO/Ni@C (Figure

S6d). Furthermore, we also noticed that the C, O, F, and Ni elements are uniformly distributed across the whole nanosheets as presented in EDS elemental mapping. All these observations suggest that F atoms are homogenous doped into the NiO matrix. Different amount of F was tried to dope into NiO matrix, which shows that the catalyst still maintains the architecture of the carbon layer surrounding the nanoparticles regardless of the content of the introduced F (Figure S7).

XRD measurements were conducted to understand the crystallinity feature of the as-prepared samples. As shown in Figure 3a, for sample $F_{0.5}$-NiO/Ni@C, the three diffraction peaks at 37.2°, 43.2°, and 62.8° are the fingerprint of NiO (JCPDF No. 47-1049), while another three pronounced peaks at 44.5∘, 51.8∘, and 76.4∘ are attributed to Ni (JCPDF No. 04-0850). Noteworthy, the diffraction peaks of NiO at 37.2° and 62.8° aredisappeared when the F-H_2SA input increased to 0.5 mmol. One possible reason behind this could be that introducing an excessive number of organic molecules (F-H_2SA) during the annealing process might have caused the reduction of NiO to metallic Ni due to the reductive nature of carbon.

No apparent carbon diffraction peak is identified in the XRD patterns, which could possibly be due to the low carbon content in the composites. Raman spectra were further carried out. As expected, two distinct vibration peaks at 1337 and 1590 cm^{-1} corresponding to the D and G bands of carbon were identified in NiO/Ni@C (Figure 3b), signifying the effective conversion of organic ligands to carbon, which is in accord with the HRTEM observation[21]. The additional peak located at 514.5 cm^{-1} is attributed to the Ni-O band of NiO[22]. No identifiable difference between F-NiO/Ni@C and NiO/Ni@C is seen in the Raman spectrum, suggesting that the introduction of F did not change the crystal structure of parent NiO. It should also be noted that the annealing temperature could also be another vital descriptor for the formation of F-NiO/Ni@C.

As shown in Figure S8 and S9, annealing temperatures below 350 °C fail to decompose the Ni(OH)$_2$, while temperatures above 550 °C lead to agglomeration of the granules, suggesting 450 °C could be the optimum annealing treatment temperature.
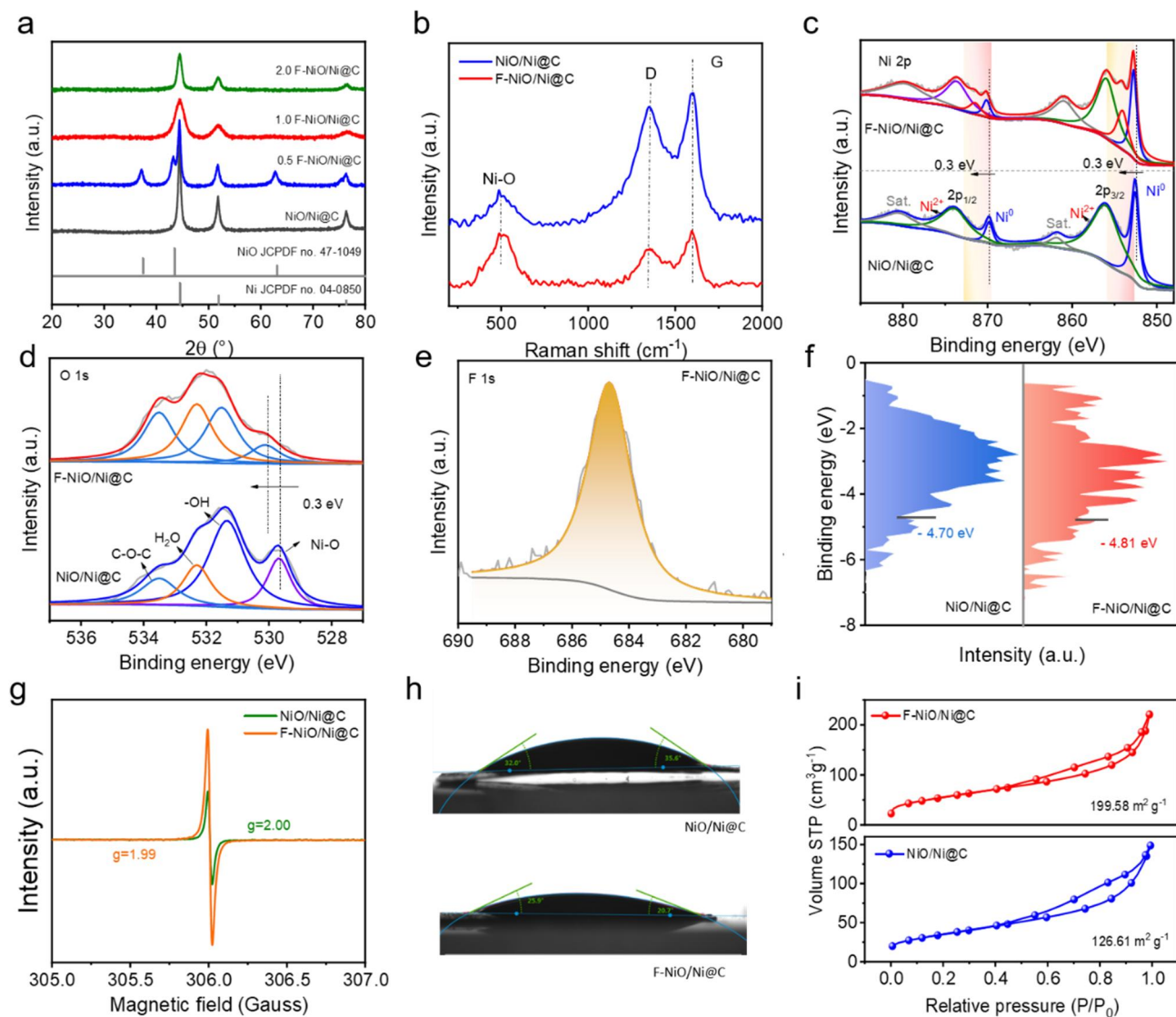

Figure 3. XRD patterns (a) and Raman spectra (b) of NiO/Ni@C and F-NiO/Ni@C. XPS high resolution spectra for Ni 2p (c) and O 1s (d) of the NiO/Ni@C and F$_x$-NiO/Ni@C. (e) F 1s of F-NiO/Ni@C. Surface valance band XPS spectra (f), ESR spectra (g), static droplets contact angles (h), and isothermal N$_2$ adsorption-desorption curves (i) of NiO/Ni@C and F$_x$-NiO/Ni@C.

X-ray photoelectron spectroscopy (XPS) was applied to understand the electronic

structure of the samples. Compared to the NiO/Ni@C, an additional weak F peak can be found in the survey spectra of F-NiO/Ni@C, again evidencing the successful doping of F into NiO matrix (Figure S10a). Figure 3c depicts the Ni 2p spectrum of NiO/Ni@C, in which the two peaks at 852.6 and 869.9 eV are related to the metallic Ni, while the two peaks at 856.2 and 874.1 eV are associated to the Ni^{2+}[23]. Besides, two other peaks at 854.1 and 871.5 eV were appeared after F doping, which could be attributed to the formed Ni-F bond [16]. It should be noted that the two Ni^0 peaks of F-NiO/Ni@C are positively shifted by 0.3 eV compared to that of NiO/Ni@C, signifying that some electrons were transferred from metallic Ni to NiO with F doping (*vide infra*). Figure 3d shows the O 1s core level of NiO/Ni@C, in which four peaks can be resolved corresponding to the lattice oxygen (529.7 eV), basic oxygen (531.5 eV), adsorbed H_2O (532.3 eV), and C-O-C (533.5 eV)[24]. Since the peak of lattice oxygen shifts to a higher binding energy after F doping, it indicates that the lattice oxygen has lost some electrons. The F1s peak with binding energy of 684.6 eV is attributed to the M⋯F interaction, suggesting that the F atom is bonded to the Ni rather than C in F-NiO/Ni@C (Figure 3e)[25]. Figure S10b shows the deconvoluted five peaks in C 1s spectra, attributed to the C=C (284.3 eV), C-C (284.8 eV), C-H (286.6 eV), and C-O (289.3 eV) components respectively, which is in accord with the characteristic of graphite. In light of all these facts, it faithfully confirms that F atom was successfully doped in the NiO lattice and varied the electron configuration of parent matrix (Figure S11). More vivid variation of the electronic state of NiO/Ni@C upon F-doping is demonstrated in photoemission spectra, in which it can be discerned that the d band centers of NiO/Ni@C and F-NiO/Ni@C are located at - 4.70 and -4.81 eV, respectively (Figure 3f). The d-band's negative shift upon F-doping suggests that the vacant antibonding states of the catalyst above the Fermi level is reduced, which may lead to favorable affinity of the reaction

intermediate on catalysts [26]. As we know, the charge imbalance and lattice distortion may contribute to the formation of vacancies in the host [27]. We then evaluate the vacancy concentration variation upon F-doping with EPR spectroscopy. As expected, the symmetric peak of F-NiO/Ni@C is stronger than that of NiO/Ni@C at g=2.002, suggesting that more oxygen vacancies are generated due to the F incorporation (Figure 3g). Apart from the catalytic active centers, the catalyst surface hydrophilicity is another key descriptor for catalytic performance[26]. Figure 3h presents the measured contact angles of the two samples. As expected, the contact angle (CA) of the electrodes of F-NiO/Ni@C is 20.7°(right), significantly smaller than that of the NiO/Ni@C (35.6° (right)), implying its superior hydrophilic nature. Additionally, N_2 measurements were done to analyze the texture of the catalysts. The Brunauer-Emmett-Teller (BET) model showed that F-NiO/Ni@C exhibit an enhanced specific surface area of $200\,\mathrm{m^2\,g^{-1}}$ compared to that of the NiO/Ni@C (i.e., $127\,\mathrm{m^2\,g^{-1}}$) (Figure 3i), signifying that F doping had a pore-generating effect (Figure S12). The increased BET surface area is predicted to expose more active sites, improving catalytic reaction kinetics.

HER performance

The HER activity of the samples was evaluated in 1 M KOH solution using a three-electrode cell setup at room temperature. The linear sweep voltammetry (LSV) curves of NF, control sample NiO/Ni@C, F-NiO/Ni@C, and commercial Pt/C were tested to investigate the effect of F modification (Figure 4a). It demonstrates that F-NiO/Ni@C achieved better HER activity with an overpotential of 46 mV to yield a current density of $10\,\mathrm{mA\,cm^{-2}}$, which is significantly lower than that of NF (220 mV), NiO/Ni@C (205 mV), and comparable to commercial Pt/C (31 mV). This preliminary control test demonstrates that the doped F has an important role in promoting HER performance. Impressively, the addressed working potential of F-NiO/Ni@C for HER outperforms

most of the recent reported transition metal-based catalysts (Figure 4g). To understand the reason for the enhanced catalytic activity of F-NiO/Ni@C, the Tafel slopes and exchange current density (j_0) were determined. As demonstrated in Figure 4b, the Tafel slope of F-NiO/Ni@C is 85 mV dec^{-1}, which is significantly lower than that of NiO/Ni@C (106 mV dec^{-1}). Likewise, the j_0 value of F-NiO/Ni@C (1.82 mA cm^{-2}) is 4.6 times that of the NiO/Ni@C (0.40 mA cm^{-2}), validating the faster reaction kinetics of F-NiO/Ni@C (Figure 4c). The electrochemical impedance spectroscopy (EIS) was also used to evaluate the HER kinetic of the samples. The charge transfer resistance (R_{ct}) value of F-NiO/Ni@C is calculated to be 1.83 Ω by fitting the Nyquist curve with the equivalent-circuit model (Figure S13), which is lower than that of NiO/Ni@C (3.99 Ω) (Figure 4d), indicating a faster charge transfer at the electrode/electrolyte interface[28]. All these results indicate that F-doping can accelerate the HER kinetic of NiO/Ni@C catalyst. Additionally, the double layer capacitance (C_{dl}) was used to assess the electrochemical surface areas (ECSAs). As shown in Figure 4e and Figure S14, it depicts that the C_{dl} value of F-NiO/Ni@C is 18.09 mF cm^{-2}, significantly larger than those of the NF (0.26 mF cm^{-2}), NiO/Ni@C (0.73 mF cm^{-2}), and Pt/C (4.69 mF cm^{-2}), indicating that F-NiO/Ni@C exposes more electroactive surface compared to other control samples[29].
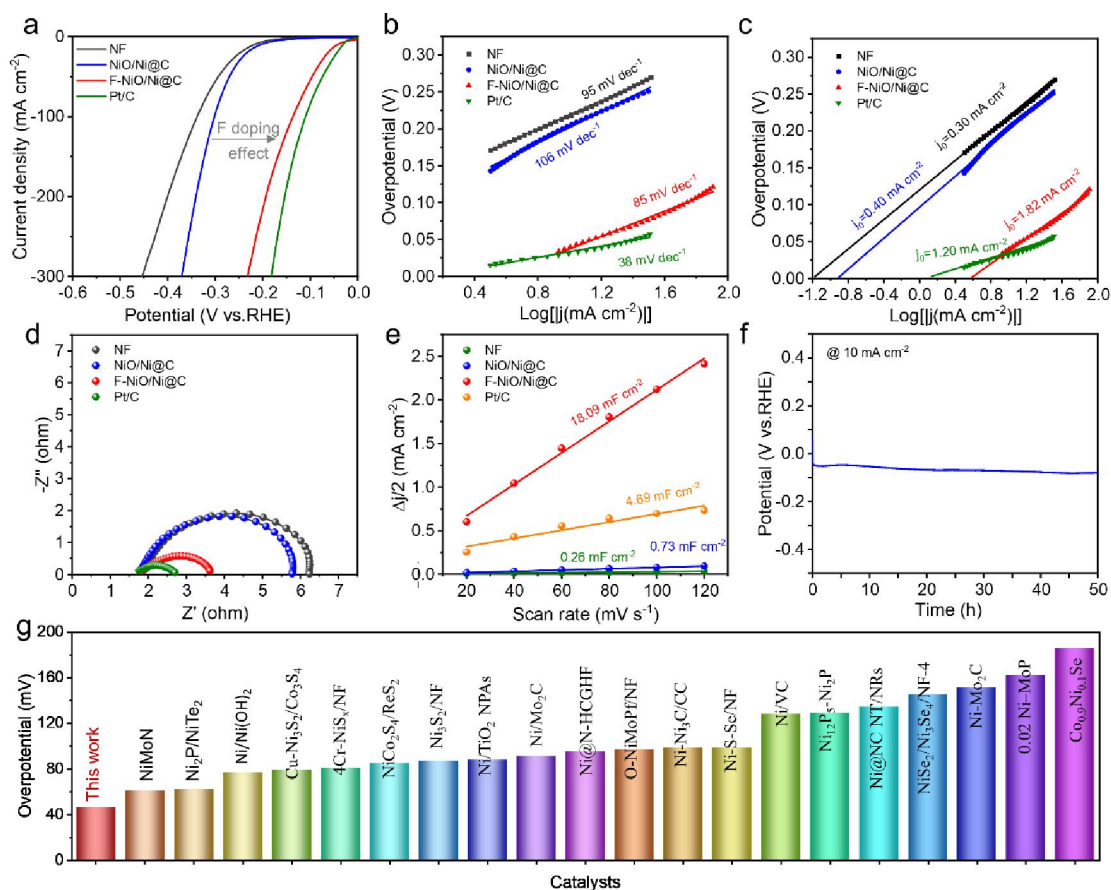
Figure 4. (a) LSV curves (with 95% iR compensation) toward HER of NF, NiO/Ni@C and F-NiO/Ni@C and Pt/C in 1 M KOH electrolyte. Tafle plots (b), exchange currentdensity (c), EIS Nyquist plots (d) and capacitive current density plots (e) of NF, NiO/Ni@C and F-NiO/Ni@C and Pt/C as a function of scan rate. (f) The chronopotentiometry tests of F-NiO/Ni@C at 10 mA cm^{-2} in 1 M KOH. (g) Comparison of F-NiO/Ni@C with the recent reported state-of-the-art catalysts at 10 mA cm^{-2} for HER.

To find the optimum F-doping, different F-doped samples were prepared and evaluated. $F_{1.0}$-NiO/Ni@C electrode delivers the lowest overpotential and Tafel plot value as can be seen from Figure S15. Moreover, the lowest R_{ct} and highest C_{dl} of $F_{1.0}$-NiO/Ni@C sample suggest that it possesses the smallest interfacial charge transfer kinetics and large amount of accessible active sites (Figure S15b,c and Figure S16). For

simplicity, hereafter the $F_{1.0}$-NiO/Ni@C is termed as F-NiO/Ni@C unless otherwise noted. We also evaluated the HER activity of the samples, annealed at different temperatures (i.e., 350, 450, and 550 °C), which are termed as F-NiO/Ni@C-350, F-NiO/Ni@C-450 and F-NiO/Ni@C-550. As expected, F-NiO/Ni@C-450 yields the smallest overpotential at the same current density (Figure S17). It should be noted that F-NiO/Ni@C exhibits robust stability in alkaline solutions, as there was only a negligible increase in potential observed after continuous operation for 50 hours. (Figure 4f). The morphology and structure of aged F-NiO/Ni@C were examined as well. Analyses of SEM (Figure S18a) and TEM images (Figure S18b) led us to show that the spent material still has cross-linked nanosheets with highly-dispersed nanostructures after the long-term HER stability test. The relatively similar XRD patterns (Figure S18c) and Raman spectra (Figure S18d) of the prototype and used samples demonstrate the excellent stability of our prepared F-NiO/Ni@C composites.

UOR performance

The urea oxidation reaction (UOR) is a catalytic anodic process occurring in urea fuel cells as well as a means for treatment of urea-rich wastewater. The UOR performance of F-NiO/Ni@C was firstly examined in 1.0 M KOH containing different concentrations of urea. As depicted in Figure S19, our as-prepared sample enables effective urea oxidation, showing an increase in current density with the concentration of urea increased from 0.1 to 0.33 M. However, the current tends decrease when the concentration of urea increased over 0.5 M. This is due to the fact that the abundant urea molecules reduced the concentration of OH$^-$ ions around the active sites, resulting in slower UOR reaction kinetics[30]. Likewise, we also evaluated the UOR catalytic activity of different F-doped samples and different annealed samples as shown in Figure S20. Figure 5a displays the LSV curves of F-NiO/Ni@C and control samples. A

working potential of 1.31 V is required to achieve a current density of 10 mA cm^{-2}, which is remarkably lower than those of the NF (1.39 V), NiO/Ni@C (1.35 V), and even commercial RuO$_2$ (1.38 V). Moreover, the corresponding Tafel slope and j$_0$ value of electrodes was determined to assess the reaction kinetics of UOR. As depicted in Figure 5b and Figure S21a, the Tafel slope value of F-NiO/Ni@C is 37 mV dec^{-1}, which is smaller than that of commercial RuO$_2$ (42 mV dec^{-1}), leaving alone the considerable advantage of F-NiO/Ni@C over NF (106 mV mV dec^{-1}) and NiO/Ni@C (98 mV dec^{-1}). The F-NiO/Ni@C exhibits a j$_0$ value of 1.79 mA cm^{-2}, which is 3.44 times that of the NiO/Ni@C (0.52 mA cm^{-2}) and much larger than NF (0.92 mA cm^{-2}) and RuO$_2$ (0.92 mA cm^{-2}) (Figure S22b). Furthermore, the C$_{dl}$ of F-NiO/Ni@C is determined to be 10.47 mF cm^{-2}, roughly 7.5 times that of the pristine NiO/Ni@C (1.39 mF cm^{-2}), demonstrating that F-doping introduces more efficient active sites for UOR (Figure S21c and Figure S22). Also, the lowest R$_{ct}$ indicates the fastest charge transfer at the electrode/electrolyte interface during the UOR process (Figure S21d).

To unravel the intricacies of the reaction kinetics governing Urea Oxidation Reaction (UOR), we conducted operando Electrochemical Impedance Spectroscopy (EIS) measurements.In the Bode phase plots of NiO/Ni@C and F-NiO/Ni@C (Figure 5c), two peaks emerge at distinct frequency ranges. The peak in the intermediate frequency range is associated with surface double-layer capacitance (DLC), while the peak in the low frequency range should be related to UOR[31]. Generally, the higher drop in the phase angle indicates faster electron transfer process[32]. For NiO/Ni@C, the phase angle in the low-frequency region is stable in the potential range of 1.26 ~ 1.34 V and exhibit sharp drop when the given potential is over 1.36 V. This is consistent with the tendency that is observed in the intermediate-frequency region, further revealing that UOR were commenced due to the accumulation of intermediates (Figure S23a)[33]. In a

sharp contrast, the phase angle for F-NiO/Ni@C drops drastically in the low-frequency region while remaining relatively stable in the mid-frequency region (1.26 ~ 1.34 V). This observation indicates that UOR occurs via a direct electron transfer pathway[33], highlighting the unique catalytic properties of our F-NiO.Ni@C composite. Furthermore, the phase angle of the low-frequency region indicating the UOR decreased earlier for sample F-NiO/Ni@C (at 1.32 V) compared to that of NiO/Ni@C (at 1.36 V), consistent with the advanced UOR activity of the F-NiO/Ni@C. In Nyquist plots, F-NiO/Ni@C shows smaller radius than NiO/Ni@C in the whole potential range, further indicating smaller charge transfer impedance of F-NiO/Ni@C compared to the parent catalyst (Figure S23c, d). Moreover, F-NiO/Ni@C exhibited remarkable stability during UOR, demonstrated by the absence of any significant potential increase even after continuous testing for 50 hours at 10 mA cm−2 (as illustrated in Figure S24). Interestingly, our prepared F-NiO/Ni@C exhibits exceptional stability during the UOR process, as demonstrated by SEM, TEM images, XRD and Raman spectroscopy characterizations. Notably, no discernible changes were observed in the aged F-NiO/Ni@C, confirming its robust stability even after prolonged UOR operation (Figure S25). **Overall urea splitting performance**

The overall urea splitting (OUS) test was developed to evaluate the possibilities of urea-assisted water electrolysis for energy-saving H_2 generation. Figure S26 demonstrates the LSV curves of F-NiO/Ni@C toward HER. Only slight performance improvement is observed with urea addition, signifying that the urea is nearly inoperative and innocuous for HER. Next, the OUS performance of a configured F-NiO/Ni@C || F-NiO/Ni@C cell was tested in 1 M KOH+ 0.33 M urea alkaline solution with F-NiO/Ni@C serving both the anode and cathode. As shown in Figure 5d, 1.37 V driving voltage is required to achieve a current density of 10 mA cm^{-2}, which

outperforms the state-of-the-art Pt/C || RuO$_2$ (1.45 V), demonstrating the advantage of our F-NiO/Ni@C composite. A chronopotentiometry test was also done to assess the stability of the as-configured OUS system at 10 mA cm^{-2}. As depicted in Figure 5e, the required potential of F-NiO/Ni@C || F-NiO/Ni@C was stable for 50 h while that of Pt/C || RuO$_2$ increased sharply in a short time, showing the potential for practical applications. The significant advantage of UOR towards energy-saving as well as its practical applications could be evidenced from the comparison between OUS and overall water splitting (OWS). A cell voltage of 1.57 V is required to yield a current density of 200 mA cm^{-2} under the framework of OUS, which is nearly 0.29 V lower than that of OWS (Figure S27), faithfully validating that replacing OER with UOR on the anode could reduce energy utilization for H$_2$ generation.

Urea-rich wastewater purification performance

Urea degradation efficiency was assessed utilizing F-NiO/Ni@C as bifunctional catalysts. We employed a modified diacetyl mono oxime-antipyrine chemical technique to assess the applicability of our catalyst for purifying urea-rich wastewater. Calibration is performed prior to the measurement by adopting standard curves of urea solution at various concentrations, as illustrated in Figure S28. The strong peak at 480 nm found in Ultra-violet spectra could be assigned to the urea fingerprint. After careful scrutiny of Figure 5f and Figure 5g, it can be easily discerned that the peak intensity significantly decreased during the 180 min testing period for the case of F-NiO/Ni@C, while NiO/Ni@C only slightly decreased. This observation informs that F-doping could effectively enhance the urea degradation of NiO/Ni@C. The advanced urea degradation capability could be more directly seen from the color change of solution before and after 180 min of catalytic treatment (Figure S29). The value of urea degradation rate of F-NiO/Ni@C is determined to be 94.86%, much higher than that of NiO/Ni@C

(23.60%), further confirming the superior performance of F-NiO/Ni@C (Figure 5h).

Moreover, even after 3 catalytic recycles, the urea degradation rate of F-NiO/Ni@C

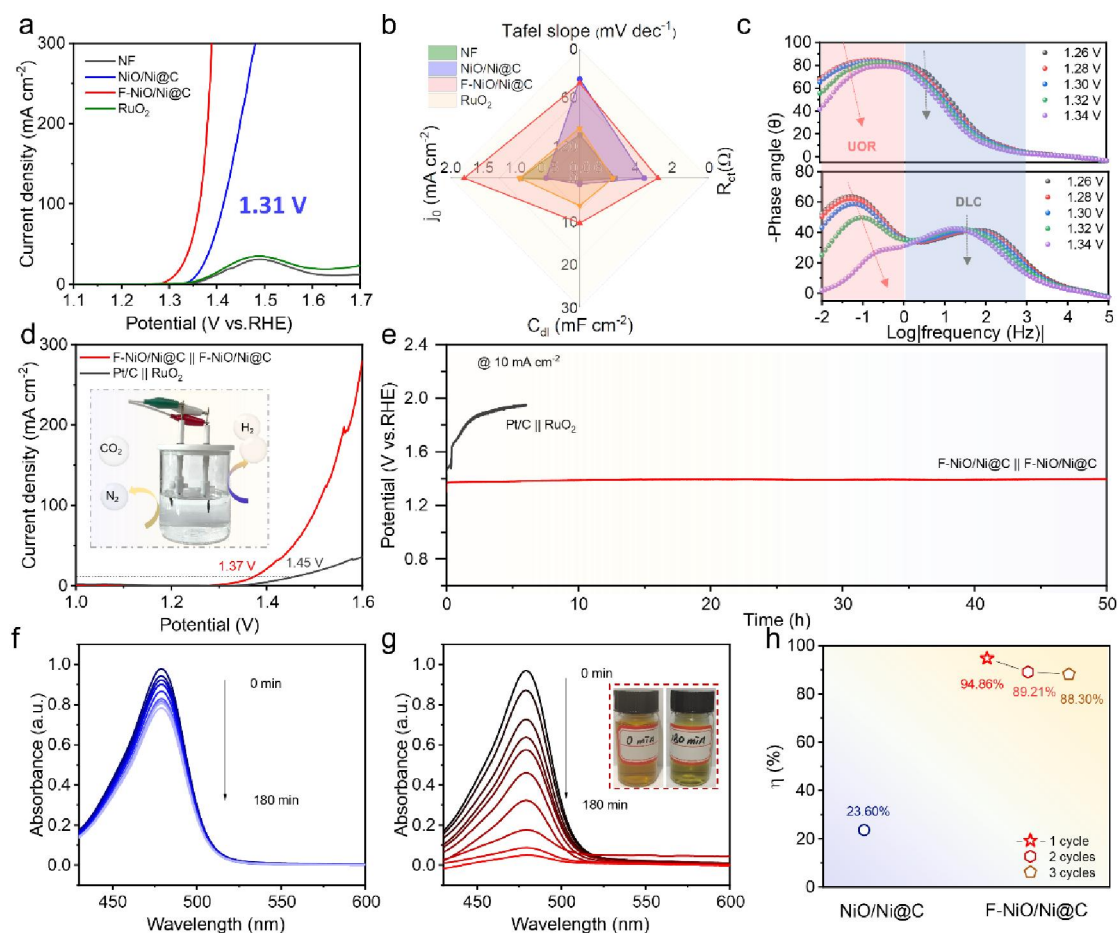was maintained at 88.3%, signifying its reusability nature (Figure 5i and Figure 30).

Figure 5. (a) LSV curves (with 95% iR compensation) toward UOR of NF, NiO/Ni@C

and F-NiO/Ni@C and Pt/C in 1 M KOH +0.33 M urea alkaline solution. (b) Radar chart

depicting Tafel plot, R_{ct}, C_{dl} and j_0 values of NF, NiO/Ni@C and F-NiO/Ni@C and

RuO$_2$. (c) Bode plots of NiO/Ni@C and F-NiO/Ni@C recorded from 1.26 to 1.34 V. (d)

LSV curves (with 95% iR compensation) of F-NiO/Ni@C || F-NiO/Ni@C and Pt/C ||

RuO$_2$ for OUS in 1 M KOH + 0.33 M urea alkaline solution. (e) Chronopotentiometry

tests of F-NiO/Ni@C || F-NiO/Ni@C and Pt/C || RuO$_2$ in 1 M KOH + 0.33 M urea

electrolyte at 10 mA cm^{-2}. Ultra-violet spectroscopy of NiO/Ni@C (f) and F-

NiO/Ni@C (g) during the urea degradation from 0 to 180 min in every 20 min. (h) The

values of urea degradation of NiO/Ni@C and F-NiO/Ni@C.

Mechanism discussion

The favorable effect of F importation on the catalytic activity of NiO/Ni@C was studied through density functional theory (DFT) calculations. Hetero-junction models of NiO/Ni, F-NiO/Ni, and F-NiO/Ni@C were constructed and analyzed as shown in Figure S31 and S32. The interaction energy of the carbon layer with the surface of NiO/Ni and F-NiO/Ni is -10.15 and -10.12 eV, respectively. Such small difference suggests that F-doping does not influence the interaction between NiO/Ni and the carbon layer (Figure S32). The electron localization function (ELF) was studied to acquire a better understanding of the bonding behavior of NiO/Ni and F-NiO/Ni. In general, ELF values of 1.00 and 0.50 correspond the scenarios that electrons are entirely localized and entirely delocalized, respectively, while the value close to 0.00 indicates an extremely low charge density[34]. The ELF map of NiO/Ni@C in Figure 6a shows that the electron density is reduced on the Ni and accumulated on the NiO, demonstrating the spontaneous electron transfer from Ni to NiO. Noteworthy, we noticed that when O atoms are replaced by F atoms in NiO, the corresponding electronic state varies from localized to complete delocalized status, which is beneficial for the electron transfer in the heterojunction. Additionally, the complete delocalization of electrons might enhance connection between the Ni and F atoms, leading to strong stability of F-NiO/Ni@C structure[35]. The negative electrostatic difference potential (EDP) was further plotted to understand electronic interaction process at multiple heterogeneous interfaces (Figure 6b). Compared to the NiO/Ni@C, the Ni part of F-NiO/Ni@C (0 to 6 Å) shows more positive electrostatic potential, while that of NiO part (10 to 15 Å) is more negative, which results in lower potential difference and favors

the electron transfer at the interface[36]. In addition, F-NiO in F-NiO/Ni@C shows higher partial density of states (PDOS) than that of NiO in NiO/Ni@C (Figure 6c), signifying that some electrons were transferred from Ni to NiO after F doping, which is in line with the aforementioned XPS results . The reason could be the fact that F-doping creates lots of oxygen defects (Figure 3f), making F-NiO a better conductor for electrons than pure NiO. Since the density of states (DOS) near the E_F of NiO/Ni@C and F-NiO/Ni@C are both originating from the d-orbits, we quantized the DOS of catalysts to d-band center (E_d) (Figure S33). The results show that the E_d of F-NiO/Ni@C (−0.66 eV) was far away from the Fermi level compared to the case of NiO/Ni@C (−0.64 eV), reducing the affinity of intermediates on catalyst, which is vital for the desorption of gaseous product[37]. From these findings, it can be concluded that F-doping facilitates the electron transfer from Ni to NiO, in turn redistributing the electron density of states and improving the stability of NiO/Ni@C.

During the HER catalysis process, its strong bonding of H_2O^* is required to facilitate the Volmer step, as well as a balanced reaction-barrier for H^* absorption and H_2 desorption[38]. Since the Ni, NiO, and C are all potential functional species, various adsorption configurations were examined (Figure S34 and S35). For the case of NiO/Ni@C, the metal Ni sites shows superior activity with the most negative H_2O adsorption Gibbs free energy (ΔG_{H2O*}) of -1.26 eV (Figure 6d), and holds a smallest hydrogen adsorption Gibbs free energy (ΔG_{H*}) of -0.25 eV (Figure 6e). After F incorporation, the active sites of H_2O^* and H^* adsorption are altered to the Ni sites in F-NiO due to the electron redistribution. Impressively, the ΔG_{H*} of the Ni sites in F-NiO is only -0.07 eV, much closer to ideal ΔG_{H*} of 0 eV compared to all the active sites in NiO/Ni@C, favoring the H_2 release. As such, we can conclude that the F-doping could activate the NiO species by adjusting electronic structure and endow the F-
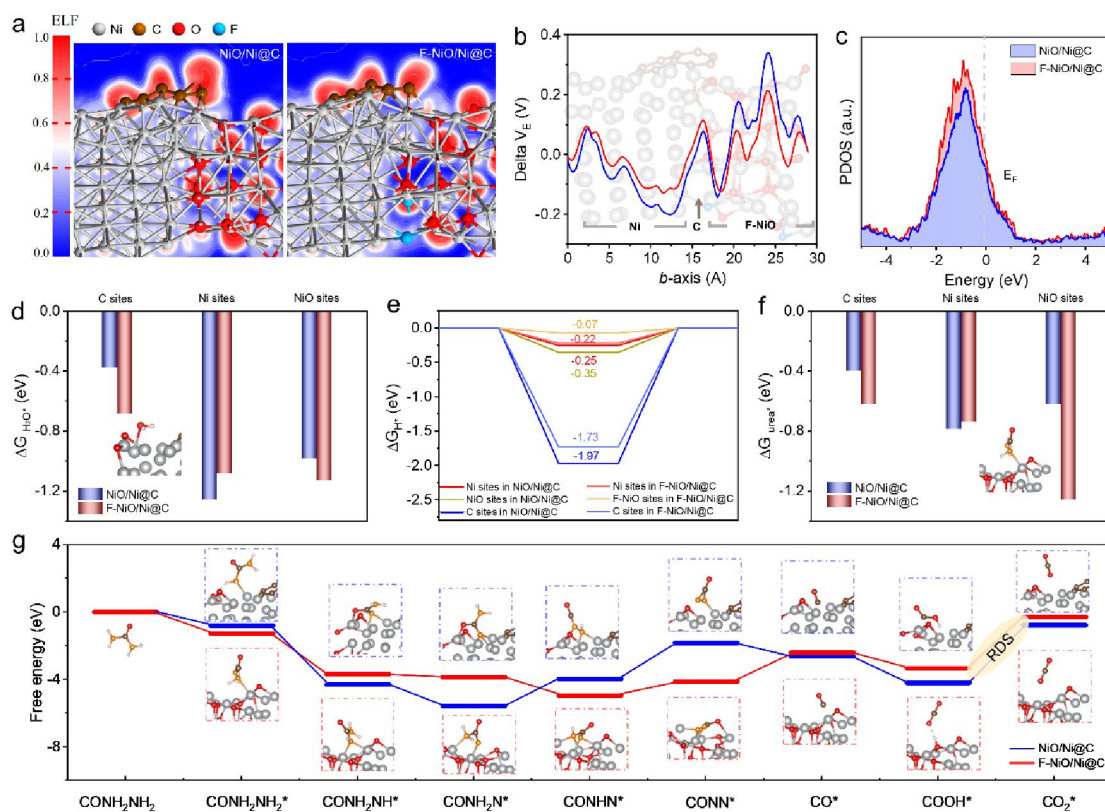
NiO/Ni@C with a faster HER kinetics.

Figure 6. (a) ELF maps of the heterostructured NiO/Ni@C and F-NiO/Ni@C, in which the gray, brown, red, and blue balls represent Ni, C, O and F, respectively. The red and blue regions refer to the highest (1.0) and lowest value (0.0) of ELF, illustrating the electron gain and electron loss, respectively. (b) The average projection plots of the electrostatic difference potential of NiO/Ni@C and F-NiO/Ni@C along the c-axis. (c) Calculated PDOS of NiO in NiO/Ni@C and F-NiO in F-NiO/Ni@C. (d) The adsorption free energy of water (ΔG_{H_2O}) on various sites of NiO/Ni@C and F-NiO/Ni@C. (e) Free energy diagram of H* adsorption on various sites of NiO/Ni@C and F-NiO/Ni@C. (f) The adsorption free energy of urea (ΔG_{urea}) on various sites of NiO/Ni@C and F-NiO/Ni@C. (g) Free energy profiles of NiO/Ni@C and F-NiO/Ni@C for UOR.

For UOR, there are two possible catalytic reaction pathways. One is a direct six-electron process ($CO(NH_2)_2 + 6OH^- \rightarrow N_2 + CO_2 + 5H_2O + 6e^-$), and a two-stage

reaction pathway involving a conversion process ($CO(NH_2)_2 + H_2O \rightarrow CO_2 + 2NH_3$) and an electron transfer process ($2NH_3 + 6OH^- \rightarrow N_2 + 6H_2O + 6e^-$)[4]. Since NH_3 will transform to NH_4^+ in the alkaline solution, the UOR reaction pathway can be distinguished based on whether NH_4^+ were generated during the reaction process. As predicated by the results of indiophenol blue spectrophotometry and ionic ammonia electrode detection (Figures S36 and S37), no trace of NH_4^+ was found, evidencing that the UOR in this study followed the direct six-electron process. The optimized structure of various adsorption intermediate on the NiO/Ni@C and F-NiO/Ni@C surface are displayed in Figure S38 and Figure S39. As revealed in Figure 6f, the adsorption Gibbs free energy of urea (ΔG_{urea*}) for C, metal Ni and Ni of NiO sites in the NiO/Ni@C is -0.40, -0.79 and -0.62 eV, respectively, implying that metal Ni sites are the main active sites for UOR. In the case of F-NiO/Ni@C, the ΔG_{urea*} of Ni sites in F-NiO (-1.26 eV) is more negative than that of metal Ni (-0.74 eV) and C sites (-0.62 eV), informing the active sites for UOR should be Ni sites of F-NiO. By comparison, we also found that the ΔG_{urea*} of F-NiO/Ni@C is much lower than the pristine NiO/Ni@C, signifying that F-doping endows favorable urea adsorption on the catalyst. Further, we also calculated the stepwise dehydrogenation process of urea molecule as shown in in Figure 6g. Free energy change in Figure 6g confirms that the dehydrogenation of COOH* to CO_2* is the rate-determining step (RDS) for both NiO/Ni@C and F-NiO/Ni@C. To our delight, the energy barrier of RDS is reduced from 3.42 to 3.05 eV after F-doping. The dynamic process of the COOH* absorption on the NiO/Ni@C and F-NiO/Ni@C surface was displayed in supporting information for better understanding the reduction of energy barrier. Different from the COOH* dehydrogenation of COOH* + OH* $\rightarrow$ COO* + H_2O in the case of NiO/Ni@C, the F-Ni-O structure in F-NiO/Ni@C allows obtaining H atom from COOH* directly, and release CO_2 molecule simultaneously, enabling fast

UOR catalytic kinetics. On this occasion, we can predicate that F-doping can enhance the urea adsorption, reduce the energy barrier of RDS and accelerate the CO_2 desorption, thereby improving the UOR activity of NiO/Ni@C.

Conclusion

In summary, we have designed a viable organic-inorganic hybrid strategy for simultaneous F-doping and multiple heterostructure formation. According to thorough characterization experiments and DFT calculations, F-doping increases electron delocalization, promoting electron transport from Ni to NiO and lowering the d band center of the NiO/Ni@C catalyst. This optimized electron state endows F-NiO/Ni@C with an accelerated HER kinetics and reduced energy barrier for urea dehydrogenation. As a result, the F-NiO/Ni@C needs a small overpotential of 46 mV for HER and 1.31 V for UOR to achieve a current density of 10 mA cm^2 in alkaline media, indicating that it is a bifunctional catalyst for overall urea splitting. Since the required voltage of the F-NiO/Ni@C || F-NiO/Ni@C cell to obtain a current density of 10 mA cm^{-2} is 80 mV lower than that of the state-of-the-art Pt/C || RuO_2 cell, F-NiO/Ni@C is validated as a promising precious-metal free catalyst for energy-saving H_2 generation. Furthermore, the F-NiO/Ni@C exhibits a 94.86% urea degradation rate, showing its potential as an efficient catalyst for urea-rich wastewater purification.

Supporting Information

Supporting Information is available from the Wiley Online Library or from the author.

Conflict of Interest

The authors declare no conflict of interest.

Data Availability Statement

The data that support the findings of this study are available in the supplementary material of this article.

Keywords

heterogeneous structure, anion doping, hydrogen production, urea oxidation reaction, urea-rich water purification.

References

[1] a) T. J. A, Science, 2004, 305, 972; b)S. Chu, A. Majumdar, *Nature* **2012**, 488, 294.

[2] H. Yu, S. Zhu, Y. Hao, Y. M. Chang, L. Li, J. Ma, H. Y. Chen, M. Shao, S. Peng, *Adv. Funct. Mater.* **2023**, 2212811.

[3] a) W. Xiang, N. Yang, X. Li, J. Linnemann, U. Hagemann, O. Ruediger, M.

Heidelmann, T. Falk, M. Aramini, S. DeBeer, M. Muhler, K. Tschulik, T. Li, *Nat. Commun.* **2022**, 13, 179; b)X. Wang, S. Xi, P. Huang, Y. Du, H. Zhong, Q. Wang, A. Borgna, Y. W. Zhang, Z. Wang, H. Wang, Z. G. Yu, W. S. V. Lee, J. Xue, *Nature* **2022**, 611, 702.

[4] S.-K. Geng, Y. Zheng, S.-Q. Li, H. Su, X. Zhao, J. Hu, H.-B. Shu, M. Jaroniec, P. Chen, Q.-H. Liu, S.-Z. Qiao, *Nature Energy* **2021**, 6, 904.

[5] a)H. Sun, L. Li, H. C. Chen, D. Duan, M. Humayun, Y. Qiu, X. Zhang, X. Ao, Y. Wu, Y. Pang, K. Huo, C. Wang, Y. Xiong, *Sci. Bull.* **2022**, 67, 1763; b) X. F. Xu, Q. M. Deng, H.-C. Chen, M. Humayun, D. L. Duan, X. Zhang, H. C. Sun, X. Ao, X. Y. Xue, A. Nikiforov, K. F. Huo, C. D. Wang, and Y. J. Xiong, *Research* **2022**, 9837109.

[6] a) H. Jiang, M. Sun, S. Wu, B. Huang, C. S. Lee, W. Zhang, *Adv. Funct. Mater.* **2021**, 31, 2104951; b) A. Kumar, X. Liu, J. Lee, B. Debnath, A. R. Jadhav, X. Shao, V. Q. Bui, Y. Hwang, Y. Liu, M. G. Kim, H. Lee, *Energy Environ. Sci.* **2021**, 14, 6494; c) L. Wang, Y. Zhu, Y. Wen, S. Li, C. Cui, F. Ni, Y. Liu, H. Lin, Y. Li, H. Peng, B. Zhang, *Angew. Chem. Int. Ed.* **2021**, 60, 10577.

[7] M. P. Browne, Z. Sofer, M. Pumera, *Energy Environ. Sci.* **2019**, 12, 41.

[8] a)B. Zhu, Z. Liang, R. Zou, *Small* **2020**, 16, e1906133; b) Z. Dong, F. Lin, Y. Yao, L. Jiao, *Adv. Energy Mater.* **2019**, 9, 1902703; c) N. Chen, Y.-X. Du, G. Zhang, W.-T. Lu, F.-F. Cao, *Nano Energy* **2021**, 81, 105605; d)J.-Y. Zhang, T. He, M. Wang, R. Qi, Y. Yan, Z. Dong, H. Liu, H. Wang, B. Y. Xia, *Nano Energy* **2019**, 60, 894.

[9] a)X. Xu, X. Hou, P. Du, C. Zhang, S. Zhang, H. Wang, A. Toghan, M. Huang, *Nano Research* **2022**, 15, 7124; b) C. Zhang, R. Du, J. J. Biendicho, M. Yi, K. Xiao, D. Yang, T. Zhang, X. Wang, J. Arbiol, J. Llorca, Y. Zhou, J. R. Morante, A. Cabot, *Adv. Energy Mater.* **2021**, 11, 2100432; c) Z. Jiang, S. Song, X. Zheng, X. Liang, Z. Li, H. Gu, Z. Li, Y. Wang, S. Liu, W. Chen, D. Wang, Y. Li, *J. Am. Chem. Soc.* **2022**, 144, 19619.

[10] C. Li, J.-Y. Xue, W. Zhang, F.-L. Li, H. Gu, P. Braunstein, J.-P. Lang, *Nano Research* **2022**, 1.

[11] X. Ji, Y. Zhang, Z. Ma, Y. Qiu, *ChemSusChem* **2020**, 13, 5004.

[12] a) J. Qian, X. Guo, T. Wang, P. Liu, H. Zhang, D. Gao, *Appl. Catal. B Environ.* **2019**, 250, 71; b) B. J. Rani, G. Ravi, R. Yuvakkumar, S. Ravichandran, F. Ameen, A. Al-Sabri, *J. Sol-Gel Sci. Techn.* **2018**, 89, 500; c) Z. Li, W. Niu, L. Zhou, Y. Yang, *ACS Energy Lett.* **2018**, 3, 892.

[13] a)J. Liu, D. Zhu, T. Ling, A. Vasileff, S.-Z. Qiao, *Nano Energy* **2017**, 40, 264; b) B. Xia, T. Wang, X. Jiang, J. Li, T. Zhang, P. Xi, D. Gao, D. Xue, *J. Mater. Chem. A* **2019**, 7, 4729.

[14] T. Li, J. Yin, Y. Li, Z. Tian, Y. Zhang, L. Xu, Y. Li, Y. Tang, H. Pang, J. Yang, *J. Energy Chem.* **2021**, 63, 585.

[15] a)Y Y. Zhu, X. Liu, S. Jin, H. Chen, W. Lee, M. Liu, Y. Chen, *J. Mater. Chem. A* **2019**, 7, 5875; b) N. Cao, Z. Chen, K. Zang, J. Xu, J. Zhong, J. Luo, X. Xu, G. Zheng, *Nat. Commun.* **2019**, 10, 2877.

[16] P. Zhang, Z. Liu, B. Ma, P. Li, Y. Zhou, X. Tian, *Ceram. Int.* **2021**, 47, 33843.

[17] F. L. Li, P. Wang, X. Huang, D. J. Young, H. F. Wang, P. Braunstein, J. P. Lang, *Angew. Chem. Int. Ed.* **2019**, 58, 7051.

[18] Y. Li, J. Cheng, X. Wang, Y. Liu, X. Liu, *Phys. Chem. Chem. Phys.* **2021**, 23, 26853.

[19] X. Wang, X. Wang, Q. Di, H. Zhao, B. Liang, J. Yang, *Materials* **2017**, 10, 1398.

[20] K. Dastafkan, X. Shen, R. K. Hocking, Q. Meyer, C. Zhao, *Nat. Commun.* **2023**, 14, 547.

[21] X. Xu, G. Wang, G. Wan, S. Shi, C. Hao, Y. Tang, G. Wang, *Chem. Eng. J.* **2020**, 382, 122980.

[22] N. A. Sagui, P. Strom, T. Edvinsson, I. Bayrak Pehlivan, *ACS Catal.* **2022**, 12,

6506.

[23] C. Wang, Y. Tian, Y. Gu, K.-H. Xue, H. Sun, X. Miao, L. Dai, *Nano Energy* **2021**, 85, 106030.

[24] Y. Sun, Z. Xue, Q. Liu, Y. Jia, Y. Li, K. Liu, Y. Lin, M. Liu, G. Li, C. Y. Su, *Nat. Commun.* **2021**, 12, 1369.

[25] a) S. Ippili, V. Jella, J. M. Lee, J.-S. Jung, D.-H. Lee, T.-Y. Yang, S.-G. Yoon, *J. Mater. Chem. A* **2022**, 10, 22067; b) X. Fan, Y. Liu, S. Chen, J. Shi, J. Wang, A. Fan, W. Zan, S. Li, W. A. Goddard, 3rd, X. M. Zhang, *Nat. Commun.* **2018**, 9, 1809.

[26] H. Sun, L. Li, M. Humayun, H. Zhang, Y. Bo, X. Ao, X. Xu, K. Chen, K. Ostrikov, K. Huo, W. Zhang, C. Wang, Y. Xiong, *Appl. Catal. B Environ.* **2022**, 305, 121088.

[27] Y. Tong, P. Chen, M. Zhang, T. Zhou, L. Zhang, W. Chu, C. Wu, Y. Xie, *ACS Catalysis* **2017**, 8, 1.

[28] R. Song, J. Han, M. Okugawa, R. Belosludov, T. Wada, J. Jiang, D. Wei, A. Kudo, Y. Tian, M. Chen, H. Kato, *Nat. Commun.* **2022**, 13, 5157.

[29] T. Zhao, X. Shen, Y. Wang, R. K. Hocking, Y. Li, C. Rong, K. Dastafkan, Z. Su, C. Zhao, *Adv. Funct. Mater.* **2021**, 31, 2100614.

[30] V. Vedharathinam, G. G. Botte, *Electrochim. Acta* **2012**, 81, 292.

[31] W. Chen, C. Xie, Y. Wang, Y. Zou, C.-L. Dong, Y.-C. Huang, Z. Xiao, Z. Wei, S. Du, C. Chen, B. Zhou, J. Ma, S. Wang, *Chem* **2020**, 6, 2974.

[32] D. Li, Y. Zhang, X. Zhou, C. Huang, Y. Wen, L. Liu, Q. Li, Y. Xu, Y. Wu, Q. Ruan, Y. Ma, F. Xiong, D. Xiao, P. Liu, G. Wang, B. Mehrjou, B. Wang, H. Li, R. Chen, H. Ni, Z. Zeng, P. K. Chu, *J. Energy Chem.* **2022**, 71, 150.

[33] D. Li, X. Zhou, L. Liu, Q. Ruan, X. Zhang, B. Wang, F. Xiong, C. Huang, P. K. Chu, *Appl. Catal. B Environ.* **2023**, 324, 122240.

[34] S. Zhang, Q. Wang, Y. Kawazoe, P. Jena, *J. Am. Chem. Soc.* **2013**, 135, 18216.

[35] H. Zhang, Y. Li, J. Hou, K. Tu, Z. Chen, *J. Am. Chem. Soc.* **2016**, 138, 5644.

[36] Y. Yu, S. Gao, S. Hu, *J. Alloys Compd.* **2021**, 883, 160902.

[37] Y. Shi, Z. R. Ma, Y. Y. Xiao, Y. C. Yin, W. M. Huang, Z. C. Huang, Y. Z. Zheng, F. Y. Mu, R. Huang, G. Y. Shi, Y. Y. Sun, X. H. Xia, W. Chen, *Nat. Commun.* **2021**, 12, 3021.

[38] L. Deng, F. Hu, M. Ma, S. C. Huang, Y. Xiong, H. Y. Chen, L. Li, S. Peng, *Angew. Chem. Int. Ed.* **2021**, 60, 22276.